

JGR Atmospheres

RESEARCH ARTICLE

10.1029/2018JD030000

Key Points:

- ECMWF operational and ERA5 data show moist bias (14–17%) in UTLS water vapor compared to cryogenic frostpoint hygrometer (CFH)
- ERA-Interim data shows dry bias (14–30%) in UTLS water vapor compared to CFH
- New ERA5 reanalysis provides an improved representation of UTLS water vapor compared to ERA-Interim reanalysis

Supporting Information:

- Supporting Information S1

Correspondence to:

S. Brunamonti,
simone.brunamonti@env.ethz.ch

Citation:

Brunamonti, S., Füzér, L., Jorge, T., Poltera, Y., Oelsner, P., Meier, S., et al. (2019). Water vapor in the Asian summer monsoon anticyclone: Comparison of balloon-borne measurements and ECMWF data. *Journal of Geophysical Research: Atmospheres*, 124, 7053–7068. <https://doi.org/10.1029/2018JD030000>







Received 15 NOV 2018

Accepted 6 JUN 2019

Accepted article online 20 JUN 2019

Published online 11 JUL 2019

Water Vapor in the Asian Summer Monsoon Anticyclone: Comparison of Balloon-Borne Measurements and ECMWF Data

S. Brunamonti¹ , L. Füzér¹, T. Jorge¹, Y. Poltera¹, P. Oelsner² , S. Meier², R. Dirksen², M. Naja³, S. Fadnavis⁴ , J. Karmacharya⁵ , F. G. Wienhold¹ , B. P. Luo¹, H. Wernli¹ , and T. Peter¹

¹Institute for Atmospheric and Climate Science (IAC), Swiss Federal Institute of Technology (ETH), Zürich, Switzerland,

²Deutscher Wetterdienst (DWD)/GCOS Reference Upper Air Network (GRUAN) Lead Center, Lindenberg, Germany,

³Aryabhata Research Institute of Observational Sciences (ARIES), Nainital, India, ⁴Indian Institute of Tropical Meteorology (IITM), Pune, India, ⁵Meteorological Forecasting Division, Department of Hydrology and Meteorology (DHM), Kathmandu, Nepal

Abstract Water vapor (H₂O) is the strongest greenhouse gas in our atmosphere. Hence, accurate measurements and a correct representation in global models of H₂O in the upper troposphere/lower stratosphere (UTLS) are important for understanding and projecting climate. Here we compare balloon-borne measurements of UTLS H₂O, performed by cryogenic frostpoint hygrometers (CFH) and meteorological radiosondes (Vaisala RS41) during two intensive field campaigns in the Asian summer monsoon anticyclone region, with humidity data from three products of the European Centre for Medium-range Weather Forecasts (ECMWF): operational analysis and forecast (termed OPERA), ERA-Interim reanalysis, and the newly released ERA5 reanalysis. Taking CFH as a reference, we show that OPERA and ERA5 provide a more accurate representation of UTLS H₂O than ERA-Interim. In particular, OPERA and ERA5 similarly overestimate H₂O mixing ratios by on average 0.7–0.8 ppmv (14–15%) and 0.7–0.9 ppmv (15–17%) at pressures 60–100 hPa, respectively, and both provide a good representation of the observed vertical distribution (including fine structures) and natural variability of UTLS H₂O. In contrast, ERA-Interim underestimates UTLS H₂O by 0.6–1.7 ppmv (14–30%), and it fails to capture relevant features of the vertical distribution of UTLS H₂O. At pressures (p) lower than 60 hPa, all three ECMWF products are in good agreement with CFH. Humidity measurements by RS41 show an average dry bias of 0.1–0.5 ppmv (3–9%) compared to CFH for 60–100 hPa, and a moist bias increasing with altitude for $p < 60$ hPa, exceeding 100% for $p < 40$ hPa.

1. Introduction

Water vapor (H₂O) is a natural component of the Earth's atmosphere and a major driver of weather and climate. Its mixing ratio in the atmosphere varies from a few percent units close to the surface to a few parts per million by volume (ppmv) in the stratosphere. It plays a fundamental role in microphysical processes (cloud formation), chemistry (e.g., controlling the lifetime of water-soluble pollutants), and the radiative budget of the atmosphere (both via direct radiative forcing and feedbacks on cloud formation). Water vapor is the strongest greenhouse gas in the atmosphere, and it has been shown that even changes in small amounts of stratospheric H₂O can have a significant impact on the rate of global warming (Riese et al., 2012; Solomon et al., 2010). The upper troposphere/lower stratosphere (UTLS) is the altitude region where microphysical processes that determine the H₂O concentration in young stratospheric air masses (“freeze-drying”) take place (e.g., Fueglistaler et al., 2005; Holton et al., 1995; Jensen et al., 2018; Mote et al., 1996; Newell & Gould-Stewart, 1981). Hence, an accurate representation of UTLS H₂O in numerical weather forecasting models and reanalysis products is crucial for reliable future climate predictions.

Early stratospheric H₂O measurements were achieved by manually operated airborne hygrometers and led to the discovery of key features of the stratospheric circulation, such as the rapid zonal transport and slow meridional overturning commonly known as Brewer-Dobson circulation (Brewer, 1949). Later, frostpoint hygrometers were automated and miniaturized, allowing their deployment on meteorological balloons (e.g., Brewer & Dobson, 1951; Mastenbrook & Dinger, 1961; Suomi & Barret, 1952). Currently, UTLS H₂O is monitored by a large variety of techniques including remote-sensing instruments on satellites

(e.g., Randel et al., 2001; Rosenlof et al., 2001) and on ground (e.g., Vérémes et al., 2016), as well as in situ instruments on balloons (e.g., Dirksen et al., 2014; Hurst et al., 2011; Vömel et al., 2002), research aircraft (e.g. von Hobe et al., 2013; Vaughan et al., 2008), and passenger aircraft (e.g., Petzold et al., 2017). Space-borne measurements provide global coverage and multiannual data sets; however, they are limited by low vertical resolution (typically 1–4 km) in the UTLS (e.g., Hegglin et al., 2013). In contrast, in situ measurements provide high vertical resolution in the UTLS (e.g., ≈ 5 m in this work) but are typically sparse in space and time. Due to its low concentrations, large dynamic range of variability, and the extremely low temperatures, measuring UTLS H₂O is notoriously difficult. Krämer et al. (2009) show that only a careful quality check of the H₂O measurements can ensure the correct interpretation of the observations.

Modern balloon-borne measurements are commonly performed by two types of instruments: capacitive sensors, based on the thin-film capacitor technique and mounted on meteorological radiosondes (e.g., Jachowicz & Senturia, 1981); and frostpoint hygrometers, based on the chilled-mirror principle, used within more sophisticated instruments for research purposes (e.g., Hall et al., 2016; Vömel et al., 1995). Meteorological radiosondes are able to provide accurate humidity measurements in the troposphere but typically fail to provide reliable measurements in the cold and dry UTLS and stratosphere (e.g., Dirksen et al., 2014; Survo et al., 2015). Frostpoint hygrometers, instead, can maintain high accuracy (better than $\pm 10\%$ in H₂O mixing ratio) up to altitudes around 28 km (Hall et al., 2016; Vömel et al., 2007, 2016). The AquaVIT-1 intercomparison campaign (Fahey et al., 2014), testing different water vapor sensors in a stratospheric simulation chamber subject to a wide range of conditions (50- to 500-hPa, 185- to 243-K, and 0.3- to 152-ppmv H₂O), decided that there was no accepted reference, so that the absolute accuracy of the instruments could not be established and the reference value had to be taken as the ensemble mean of a core subset of instruments. While many instruments were found to differ from such a reference by 100% and more, the cryogenic frostpoint hygrometer (CFH) belongs to the set of state-of-the-art instruments, with variations smaller than $\pm 10\%$ relative to the reference value under all conditions (Fahey et al., 2014).

Here we analyze UTLS H₂O in situ measurements from both capacitive sensors and frostpoint hygrometers, flying in tandem on the same balloon payload, performed from two stations located at the southern slopes of the Himalayas during the Asian summer monsoon (ASM) seasons 2016 and 2017. The atmospheric dynamics of the Asian UTLS during the monsoon season are dominated by a strong anticyclonic circulation, known as the ASM anticyclone, which is induced by strong and persistent deep convection at the surface (e.g., Krishnamurti & Bhalme, 1976). The ASM anticyclone is known to be strongly enriched in water vapor (among other tropospheric trace gases and aerosols) due to the coupling of deep convection and horizontal confinement by the anticyclonic winds, which act as a transport barrier (e.g., Park et al., 2007; Randel & Park, 2006). Consequently, the ASM system offers an efficient pathway for the transport of pollutants and water vapor to the global stratosphere (Garny & Randel, 2016; Pan et al., 2016; Randel et al., 2010). Therefore, an accurate representation of tracer transport in the Asian UTLS, including water vapor, is particularly relevant for global chemistry climate model simulations. Within the ASM region, the southern slopes of the Himalayas is known as one of the major source regions for polluted boundary layer air to the ASM anticyclone (e.g., Bergman et al., 2013; Fadnavis et al., 2013; Fu et al., 2006; Heath & Fuelberg, 2014; Pan et al., 2016). The importance of convection as a component of the upward transport renders simulation of UTLS H₂O concentrations in global models difficult, owing to the low resolution of global weather prediction models and reanalysis products (Bergman et al., 2013).

Previous comparisons of UTLS H₂O from European Centre for Medium-range Weather Forecasts (ECMWF) operational data and ERA-Interim with passenger aircraft measurements showed that the model data often exhibit a moist bias at altitudes 9–12 km in the extratropical lower stratosphere (Dyroff et al., 2015). High-altitude research aircraft measurements (tropics and extratropics, up to 18 km altitude), instead, suggest a dry bias in the UTLS, with the model overestimating the frequency of occurrence of low H₂O mixing ratios and underestimating the frequency of occurrence of high H₂O mixing ratios compared to the observations (Kunz et al., 2014). Direct comparisons of ECMWF humidity data with frostpoint hygrometer measurements are limited in the literature (e.g., Thölix et al., 2016, but not focusing on the UTLS). To our knowledge, no comparison of ECMWF humidity data and balloon-borne measurements of UTLS H₂O in the ASM anticyclone exists, despite its importance as potential entry region into the global stratosphere.

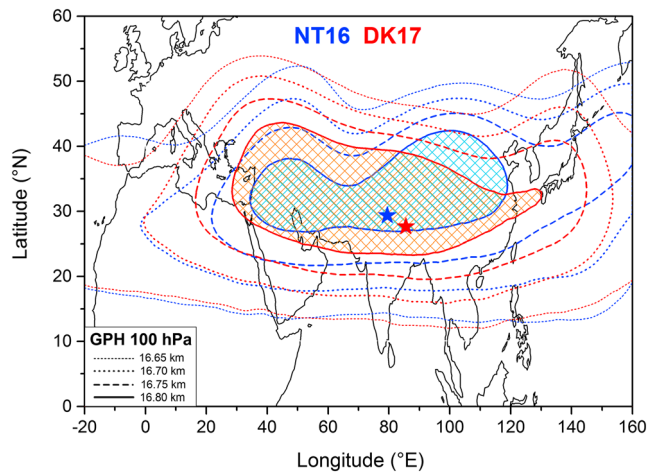


Figure 1. Average contours of geopotential height (GPH) at 100 hPa from European Centre for Medium-range Weather Forecasts analysis data (horizontal resolution $1^\circ \times 1^\circ$) during the NT16 (blue) and DK17 (red) campaign periods. Four GPH contours are shown for each campaign period, namely, 16.65 km (thin dotted lines), 16.70 km (thick dotted), 16.75 km (dashed), and 16.80 km (solid). In addition, the areas of GPH > 16.8 km are highlighted by colored hatching. The average GPH fields are calculated for the same time periods used for the temperature comparison (see section 3). The locations of Nainital and Dhulikhel are identified by a blue and red star, respectively.

Taking CFH as a reference, the aim of this work is to assess the accuracy of UTLS H_2O in the ASM anticyclone (in terms of mean values as well as the extent of natural variability) provided by ECMWF operational, ERA-Interim reanalysis, and the newly released ERA5 reanalysis data. In addition, the CFH measurements are compared to humidity measurements by Vaisala RS41 meteorological radiosondes, in order to determine to what altitude in the UTLS the humidity measurements by capacitive sensor are still in reasonable agreement with frostpoint hygrometers. The observational and model data sets are described in detail in sections 2 and 3, respectively. Comparison of measured and modeled temperature, H_2O mixing ratio, and ice saturation are discussed in sections 4 (observations vs. model) and 5 (radiosondes vs. frostpoint hygrometers), and the results are summarized in section 6.

2. Observations

The measurements analyzed in this paper were performed within the StratoClim project from the stations of Nainital, India (29.35°N , 79.46°E), during August 2016 (termed NT16) and Dhulikhel, Nepal (27.62°N , 85.54°E), during July–August 2017 (termed DK17). Both sites are located along the southern slope of Himalayas, a region subject to frequent orographically enhanced deep convection during the monsoon season (e.g., Vellore et al., 2016). Figure 1 shows selected contours of average geopotential height at 100 hPa from ECMWF analysis data during the two campaign periods.

Nainital and Dhulikhel are both found in the region of highest geopotential height during their respective operating periods, hence near the center of the ASM anticyclone (Figure 1). Besides H_2O and temperature, the campaigns also featured balloon-borne measurements of ozone and aerosol backscatter. An overview of all the data is given by Brunamonti et al. (2018). Here we focus on water vapor measurements by RS41-SGP radiosondes (hereafter “RS41”) manufactured by Vaisala, Finland (Vaisala, 2017), and by CFHs manufactured by En-Sci, United States (Vömel et al., 2007, 2016).

Humidity measurements by RS41 are based on the thin-film capacitor technique (e.g., Jachowicz & Senturia, 1981), in which relative humidity (RH) over liquid water is inferred from changes in the surface capacitance of a thin polymer dielectric film deposited over planar electrodes. Capacitive sensors can provide accurate measurements over a wide range of humidities, but the nonlinearity of the conductivity response leads to large uncertainties at low RHs and low temperatures (Jachowicz & Senturia, 1981). RS41 is the new model of Vaisala radiosonde and is currently replacing the older model (RS92) in monitoring networks, such as the GCOS Reference Upper Air Network (e.g., Dirksen et al., 2014), as well as in operational observational networks. RS41 has a manufacturer-specified resolution of 0.1% for RH and a combined uncertainty in soundings of 4% RH (Vaisala, 2017). In this study, we use corrected RH data obtained by the DigiCORA MW41 software (Vaisala, 2014) that, in addition to the ground check zero humidity correction, applies an empirical correction for time lag and accounts for the measured temperature of the heated humidity sensor (Vaisala, 2017; as also described by Miloshevich et al., 2009, for RS92). The time lag correction is necessary to compensate the error caused by the slow sensor response at low temperatures (Miloshevich et al., 2009), while the heating of the humidity sensor serves to prevent it from icing during freezing sounding conditions. The RH data are converted to H_2O volume mixing ratio using temperature and pressure measured by RS41 and the Hardy (1998) formulation of the Wexler (1976) parameterization for saturation vapor pressure over liquid water, which is recommended for the analysis of Vaisala RH data since it is assumed in their instrumental calibration (private communication with Hannu Jauhiainen, 21 January 2019; see also Appendix A in Miloshevich et al., 2009). A recent intercomparison in the Arctic region shows that corrected RS41 data agree with CFH within $\pm 10\%$ in H_2O mixing ratio up to 15 km altitude, while corrected RS92 data exceed the 10% discrepancy already above 11 km altitude (Survo et al., 2015).

CFH is a frostpoint hygrometer based on the chilled-mirror principle (e.g., Vömel et al., 1995), in which frostpoint temperature (T_{fp}) is inferred from changes in reflectivity of a mirror coated by liquid water or ice. The

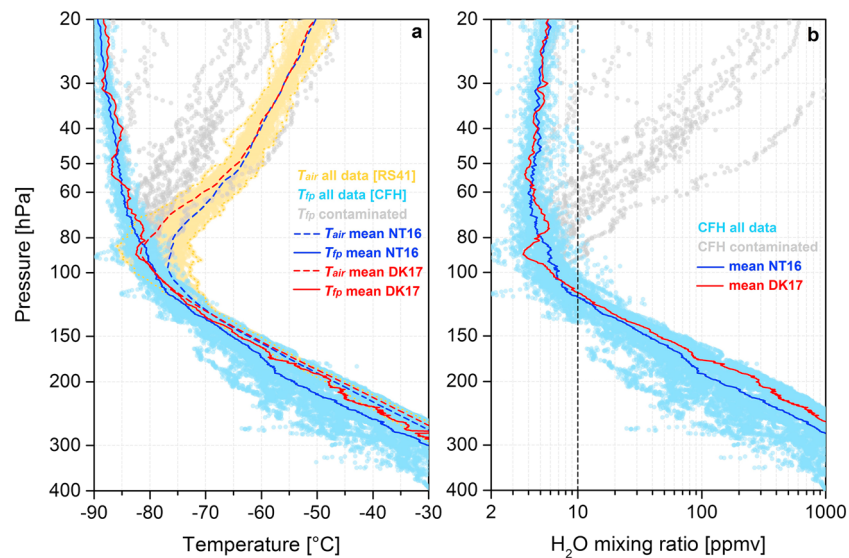


Figure 2. (a) All data points of air temperature by RS41 (T_{air} , yellow dots), frostpoint temperature by cryogenic frostpoint hygrometer (CFH; T_{fp} , light blue dots), and contaminated T_{fp} measurements by CFH (gray dots) collected during the NT16 and DK17 campaigns. Thin lines show the mean profiles of T_{air} (dashed) and T_{fp} (solid) for the NT16 (blue) and DK17 (red) campaigns. Dotted yellow lines show the minimum-maximum range of the T_{air} measurements. (b) All data points of H_2O mixing ratio by CFH (light blue dots) and contaminated H_2O mixing ratio by CFH (gray dots) collected during the NT16 and DK17 campaigns. Thin lines show the mean profiles of H_2O mixing ratio for the NT16 (blue) and DK17 (black) campaigns.

phase of the condensate depends on mirror temperature and other factors, such as mirror cleanliness, which are experimentally difficult to control (Vömel et al., 2016). For this reason, the CFH forces the condensate to freeze when the mirror temperature falls below -15°C (Vömel et al., 2007), which ensures the condensate consists of ice for all measurements analyzed in this paper. A feedback control mechanism aims at keeping the mirror reflectivity constant, meaning that the condensate layer on the mirror is kept at constant thickness, which in turn ensures that the mirror temperature equals T_{fp} at all times. A cryogenic refrigerant liquid (trifluoromethane: CHF_3 , also known as Freon R23) is used to cool the mirror. In this work, the T_{fp} measurements by CFH are converted to H_2O mixing ratios using air pressure measured by RS41 and the parameterization for saturation vapor pressure over ice by Murphy and Koop (2005). The uncertainty of CFH is estimated to be smaller than 10% in H_2O mixing ratio up to ≈ 28 km altitude (Vömel et al., 2007, 2016).

During the NT16 and DK17 campaigns, we performed in total 56 balloon soundings with RS41 and 38 with CFH, distributed as 28 RS41 and 27 CFH during NT16 (2–31 August 2016) and 28 RS41 and 11 CFH during DK17 (30 July to 12 August 2017). The soundings were made during both daytime and nighttime, following an irregular schedule mainly dictated by operational constraints. Due to known contamination artifacts of CFH (discussed in the next paragraph), we avoided starting soundings during heavy rainfall; nevertheless, a significant number of profiles sampled thick clouds. While all except one RS41 sounding in NT16 included a simultaneous CFH measurement, the majority of RS41 soundings in DK17 (17 out of 28) did not. For this reason, only the 11 RS41 soundings performed simultaneously with CFH are used for the H_2O instrumental comparison discussed in section 5, whereas all 28 RS41 soundings from DK17 are used for the temperature comparison against ECMWF data described in section 4.1. A list of all balloon soundings with dates and times of launch and notes on payload status is given in Table S1 by Brunamonti et al. (2018).

The RS41 and CFH data analyzed in this paper are ascent-only and binned in 0.5-hPa pressure intervals (corresponding to a vertical resolution of ≈ 25 m in the UTLS), which improves the signal-to-noise ratio (typically between 5% and 15–20% in H_2O mixing ratio, estimated from stratospheric data of two individual CFH profiles with high and low controller stability, respectively). The quality-check procedure applied to CFH measurements includes the rejection of contaminated data in the stratosphere, as described Brunamonti et al. (2018). This is shown in Figure 2, displaying all data and mean profiles of T_{air} measured by RS41, T_{fp}

Table 1
Summary of the Model Data Sets Used for the Comparison

Data set	ECMWF product	IFS model cycle	Output frequency	Horizontal resolution	Vertical resolution
OPERA	Operational analysis	41R2 and 43R3 ^a	6-hourly (00, 06, 12, and 18 UTC)	0.125° × 0.125°	L137
	Operational forecast		1-hourly (used at all time steps except 00, 06, 12, and 18 UTC)		
ERA-Interim	ERA-Interim Reanalysis	31R2	6-hourly (00, 06, 12, and 18 UTC)	1° × 1°	L60
ERA5	ERA5 Reanalysis	41R2	1-hourly	0.5° × 0.5°	L137

Note. ECMWF = European Centre for Medium-range Weather Forecasts; IFS = Integrated Forecasting System.

^aIFS model cycle 41R2 in use for the NT16 campaign time period and 43R3 for the DK17 campaign period (see section 3).

measured by CFH (Figure 2a), and the resulting H₂O mixing ratio from CFH (Figure 2b). The contamination occurs in a significant number of cases (five in NT16 and four in DK17), and it consists in the continuous drift with altitude of frostpoint temperatures in the stratosphere (Figure 2a, gray dots), toward values corresponding to H₂O mixing ratios of several tens or even hundreds ppmv (Figure 2b), largely exceeding the expected stratospheric background of 4–5 ppmv. Stratospheric contamination is a known artifact of frostpoint hygrometer measurements, and it can arise from a variety of sources, including water vapor outgassing from the balloon's envelope, the parachute or the load line, and icing of the inlet tubes by deposition of supercooled water droplets while passing through mixed-phase clouds (Brunamonti et al., 2018; Vömel et al., 2016). To avoid these effects, for the analysis in this paper, we do not accept stratospheric data from soundings in which H₂O mixing ratio exceeds 10 ppmv above the cold-point tropopause (CPT): in such cases, all CFH data at altitudes above the CPT are flagged as contaminated.

Pressure measurements by RS41, used as the main vertical coordinate in this work, are subject to instrumental uncertainties of ± 1.0 hPa for pressures $p > 100$ hPa and ± 0.6 hPa for $p < 100$ hPa, as specified by the manufacturer (Vaisala, 2017). For the air temperature (T_{air}) measurements by RS41 (discussed in section 4.1), the uncertainty given by the manufacturer is ± 0.3 °C for altitudes below 16 km (i.e., approximately $p > 100$ hPa) and ± 0.4 °C for altitudes higher than 16 km ($p < 100$ hPa). For the calculation of ice saturation (S_{ice}) from CFH (discussed in sections 4.3 and 5.2), we use p and T_{air} measured by RS41, T_{fp} from CFH, and the parameterization for saturation vapor pressure over ice by Murphy and Koop (2005). For stratospheric conditions ($p < 100$ hPa), the RS41 uncertainties on p and T_{air} correspond to uncertainties of about ± 0.05 ppmv on H₂O mixing ratio and ± 0.01 on S_{ice} estimated from CFH, respectively.

3. Model Data

We compare the in situ measurements described in the previous section with temperature and humidity data from three meteorological data sets of the ECMWF, namely: operational analysis and forecast (combined together as described below), the ERA-Interim reanalysis, and the newly released ERA5 reanalysis product. All these data sets are based on the Integrated Forecasting System (IFS) global model system operated by ECMWF, which is a general circulation model providing analyses and forecasts for a large set of atmospheric variables, including temperature and H₂O expressed as specific humidity (Q , i.e., mass of water vapor in a unit mass of moist air). The IFS model regularly undergoes updates in order to improve its forecast skill, for example, allowing ice supersaturated conditions in the UTLS, which has been shown to have significantly improved the representation of UTLS humidities (Tompkins et al., 2007). For the analysis and reanalysis data sets, tropospheric humidity measurements from meteorological radiosondes, aircraft, and satellite observations are also assimilated (Dyroff et al., 2015). During the time periods of our balloon campaigns, the model versions in use for operational analysis and forecast were IFS cycles 41R2 (implemented on 8 March 2016) for NT16 and 43R3 (implemented on 11 July 2017) for DK17 (see Table 1). ERA-Interim reanalyses are based on IFS cycle 31R2 (in use for operational forecast from 12 December 2006 to 5 June 2007), which is not updated in order to maintain a consistent long-term data set. An overview of this general circulation model and its assimilation methods is given by Dee et al. (2011). The ERA5 reanalysis is based on the newer IFS cycle 41R2 and provides several improvements compared to ERA-Interim, including higher spatial and temporal resolution (ECMWF, 2018).

The main characteristics of the three data sets used in this work are summarized in Table 1. All data are interpolated to regular latitude-longitude grids of $0.125^\circ \times 0.125^\circ$ for operational analysis and forecast (approximately corresponding to a horizontal resolution of 12.5 km), $1^\circ \times 1^\circ$ for ERA-Interim (≈ 100 km), and $0.5^\circ \times 0.5^\circ$ for ERA5 (≈ 50 km) using the Meteorological Archival and Retrieval System of ECMWF. The data are provided on hybrid model vertical levels versions L137 (i.e., 137 model levels from the surface to 0.01 hPa) for operational analysis and forecast and ERA5 and L60 (i.e., 60 levels from the surface to 0.1 hPa) for ERA-Interim. Operational analysis data are available at 6-hr intervals (00, 06, 12, and 18 UTC), while forecast data are available at 1-hr time resolution, resulting from two daily forecasts initialized at 00 and 12 UTC. Therefore, to obtain a data set with the highest possible time resolution (hence to increase the statistical relevance of the comparison), we combine the analysis and forecast by taking analysis data files for every time step at 00, 06, 12, and 18 UTC and forecast data files for all other time steps, from the most recent available forecast run. This means that, for every day, forecast data files initialized at 00 UTC are used for 01–11 UTC (except for 06 UTC, when analysis is used) and forecast initialized at 12 UTC for 13–23 UTC (except 18 UTC). In the following, this combined data set of analysis and forecast data will be referred to as “OPERA.” The ERA-Interim (hereafter “ERA-Interim”) and ERA5 reanalysis data sets are provided at 6-hourly and 1-hourly time resolutions, respectively.

The time periods considered for the H₂O comparison are 00 UTC 2 August 2016 to 18 UTC 31 August 2016 for NT16 and 00 UTC 3 August 2017 to 18 UTC 12 August 2017 for DK17, selected in order to coincide with the CFH measurement periods. For the temperature comparison (section 4.1), the selected time period for DK17 is 00 UTC 30 July 2017 to 18 UTC 12 August 2017, due to the fact that CFH soundings were started later with respect to RS41 during this campaign (see Table S1 in Brunamonti et al., 2018). The ECMWF data are extracted for the model grid cell where the launching sites of NT and DK are located. Since the horizontal drift of the balloons with altitude in the pressure range considered for the comparison (40–160 hPa) is about 30–40 km, which is smaller than the grid cell size of ERA-Interim and ERA5, we assume that the balloon’s ascent takes place vertically within a single grid cell (see supporting information Figure S1a). For the finer grid of OPERA, spatial sensitivity was investigated by testing the average difference between neighboring grid cells around the launching site (Figure S1b), which revealed no significant differences with respect to taking just the launch grid cell. Hence, no spatial interpolation of the model data to the balloon flight track is performed. Additional tests were carried out to check the sensitivity of the comparison when including all model time steps from the campaign periods compared to selecting only the model time steps when a balloon sounding was performed (Figure S2), showing that the differences between the two approaches are negligible. This suggests that the balloon measurements provide a statistically sufficient representation of the vertical distributions of UTLS H₂O during the measurement periods.

Finally, the specific humidity data from all ECMWF products are converted to H₂O volume mixing ratio by multiplying Q with the ratio of the molar mass of dry air (28.964 g) to the molar mass of H₂O (18.015 g) and expressed as ppmv. For the calculation of ice saturation in the model data (section 4.3), we use modeled temperature and H₂O mixing ratios and the parameterization for saturation vapor pressure over ice by Murphy and Koop (2005).

4. Model Comparison

In this section we compare temperature, H₂O mixing ratio, and ice saturation from the observational data sets of RS41 and CFH, with ECMWF model data from the three data sets introduced above (OPERA, ERA-Interim, and ERA5). The temperature comparison is useful to interpret the results of the water vapor comparison, because H₂O and T_{air} are related via the Clausius-Clapeyron relationship (i.e., the saturation vapor pressure over ice is a strong function of temperature), as shown by the “tape recorder” signal of stratospheric H₂O, which represents the ascending signature of the seasonal cycle of tropical CPT temperature (Mote et al., 1996). The comparison of S_{ice} , which is the parameter that controls cloud formation and dehydration processes in the UTLS, offers further insights for the interpretation of the H₂O comparison.

4.1. Temperature (RS41 vs. ECMWF)

Figures 3a and 3b show all temperature (T_{air}) data measured by RS41 during the NT16 (Figure 3a) and DK17 (Figure 3b) campaigns as a function of pressure for the interval 40–160 hPa, in comparison with mean

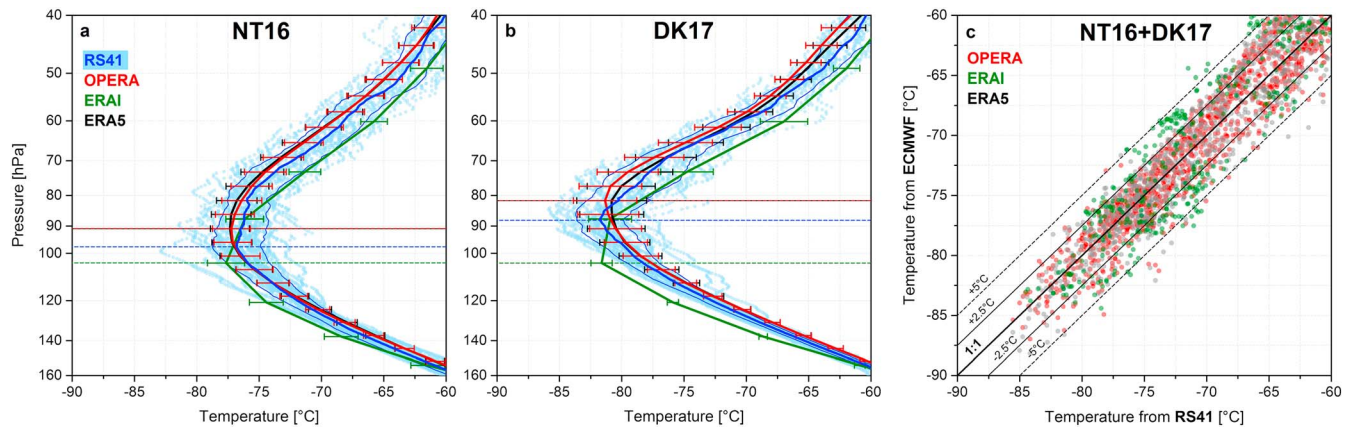


Figure 3. Temperature comparison of RS41 measurements versus ECMWF data for the NT16 and DK17 campaigns. (a, b) All temperature data points of RS41 (dots), mean profile (thick blue solid line) and standard deviation of natural variability (thin blue lines), and mean profile and standard deviation bars of OPERA (red), ERAI (green), and ERA5 (black) as a function of pressure. Horizontal dashed lines show the pressure level of the average cold-point tropopause in the different data sets. (c) Scatter plot of temperature from RS41 versus OPERA (red dots), RS41 versus ERAI (green), and RS41 versus ERA5 (gray) for the NT16 and DK17 campaign periods. Black lines show the 1:1 correspondence line (thick solid) and discrepancies by $\pm 2.5^{\circ}\text{C}$ (thin solid) and $\pm 5^{\circ}\text{C}$ (thin dashed) between the model data and the RS41 measurements.

profiles and standard deviations of the OPERA, ERAI, and ERA5 data sets. The pressure range considered in this figure (and in Figures 4, 6, and 9) encompasses 27 pressure levels of OPERA and ERA5, 9 pressure levels of ERAI, and 240 pressure bins of 0.5 hPa width for the balloon-borne measurements, according to the binning discussed in section 2. Figure 3c shows a scatter plot of T_{air} from OPERA, ERAI, and ERA5 versus T_{air} from RS41 for both campaign periods, allowing a point-by-point comparison of measured and modeled data. For the scatter plot in this figure (and in Figure 4c), the balloon data are averaged in pressure bins to represent the lower-resolution vertical grids of OPERA/ERA5 (L137) and ERAI (L60) and plotted one-by-one against the model time step closest to the considered sounding time (approximated as the closest model time step to the time when the balloon was at 100 hPa during ascent).

First, we note that significantly different UTLS temperature ranges were observed during the two campaign periods. In NT16, the tropopause region was relatively mild, and the average CPT temperature was -76.8°C (97.5 hPa, with standard deviation $\approx 2^{\circ}\text{C}$). In contrast, much lower T_{air} were observed during DK17, and the

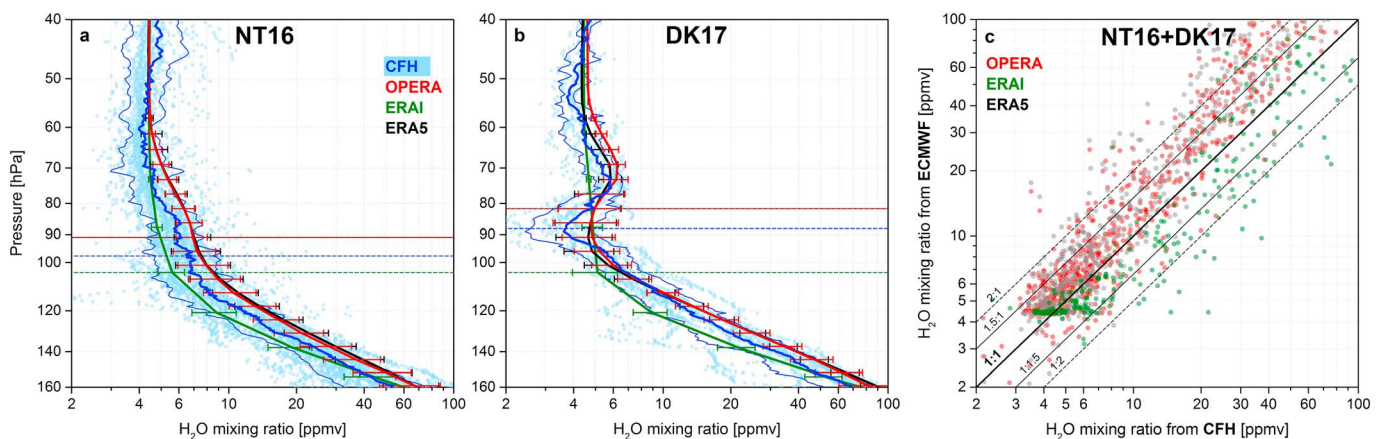


Figure 4. H_2O mixing ratio comparison of CFH measurements versus ECMWF data for the NT16 and DK17 campaigns. (a, b) All H_2O mixing ratio data points of CFH (dots), mean profile (thick blue solid line) and standard deviation of natural variability (thin blue lines), and mean profile and standard deviation bars of OPERA (red), ERAI (green), and ERA5 (black) as a function of pressure. Horizontal dashed lines show the pressure level of the average cold-point tropopause in the different data sets. (c) Scatter plot of H_2O mixing ratio from CFH versus OPERA (red dots), CFH versus ERAI (green), and CFH versus ERA5 (gray) for the NT16 and DK17 campaign periods. Black lines show the 1:1 correspondence line (thick solid) and discrepancies by $\pm 50\%$ (i.e., 1:1.5 and 1:1.5 correspondences: thin solid) and $\pm 100\%$ (i.e., 1:2 and 2:1 correspondences: thin dashed) between the model data and the CFH measurements.

average CPT was 5 K colder (-81.7°C , standard deviation $\approx 2^{\circ}\text{C}$) and ≈ 600 m higher (88 hPa) compared to NT16. Brunamonti et al. (2018) showed that these differences are mainly due to interannual variability and particularly to a period of anomalously cold UTLS occurring in the ASM anticyclone after 3 August 2017 and persisting on a large scale.

Figures 3a and 3b show that the observed interannual variability of UTLS temperature is well captured by all ECMWF products, exhibiting a colder CPT in 2017 than in 2016. In particular, the average CPT temperatures for NT16 are -77.2 and -77.3°C (91 hPa) in OPERA and ERA5, respectively, and -77.7°C (104 hPa) in ERAI while, for DK17, -81.3 and -80.8°C (81.6 hPa) in OPERA and ERA5 and -81.6°C (104 hPa) in ERAI. When the high-resolution RS41 data are binned to the low-resolution pressure grids of ECMWF, the RS41 CPT is found on the 96 hPa (NT16) and 86 hPa (DK17) pressure levels for the L137 model configuration and 87.6 hPa for both NT16 and DK17 for the L60 model configuration. Thus, OPERA and ERA5 show the tendency to overestimate CPT height by about 5 hPa (≈ 300 m) compared to the measurements, while ERAI underestimates it by about 16 hPa (≈ 900 m).

OPERA and ERA5 achieve excellent representations of UTLS T_{air} , with averages generally within $\pm 1^{\circ}\text{C}$ of RS41 measurements in both campaign periods (Figures 3a and 3b). However, they also show a slight cold bias in the lower stratosphere, with discrepancies up to $\approx 2.5^{\circ}\text{C}$ compared to RS41 (Figure 3c). OPERA and ERA5 show nearly identical temperature profiles and standard deviations in NT16, which is expected since these two products are based on the same IFS model version (see Table 1). Slightly higher T_{air} ($\approx 1^{\circ}\text{C}$) in ERA5 compared to OPERA for $p < 90$ hPa in DK17 (Figure 3b) is the only noticeable difference between these two data sets, likely due to the introduction of IFS cycle 43R3 in OPERA before the DK17 campaign (see Table 1). ERAI shows a systematic cold bias in the upper troposphere ($p > 100$ hPa) and a warm bias in the lower stratosphere ($p < 100$ hPa), with discrepancies sometimes as large as 5°C with respect to the RS41 measurements.

4.2. H₂O Mixing Ratio (CFH vs. ECMWF)

4.2.1. Vertical Profiles and Correlations

Figures 4a and 4b show all CFH measurements of H₂O mixing ratio as a function of pressure for the interval 40–160 hPa, in comparison with mean profiles and standard deviation ranges of OPERA, ERAI, and ERA5. The corresponding scatter plot of H₂O mixing ratio from CFH versus the three ECMWF products is shown in Figure 4c.

As discussed in Brunamonti et al. (2018), different vertical profiles of UTLS H₂O are observed during the two campaigns. In NT16, average H₂O mixing ratio steadily decrease with altitude up to approximately 60 hPa, followed by a slight increase with altitude due to the oxidation of methane. Conversely, the average H₂O mixing ratio profile in DK17 shows a minimum at the CPT and a local isolated maximum in the lower stratosphere (70–80 hPa). This feature, which is not in accordance with the climatological structure of UTLS H₂O (e.g., Pan et al., 2014), is conceivably due to deep convective updrafts overshooting the CPT in the ASM anticyclone, injecting ice crystals directly above the CPT, which then sublimate and hence hydrate the lower stratosphere (Brunamonti et al., 2018).

Similarly as for T_{air} , OPERA and ERA5 show almost identical vertical distributions of UTLS H₂O (Figures 4a and 4b). During both the NT16 and DK17 campaign periods, OPERA and ERA5 systematically display a slight overestimation of UTLS H₂O compared to CFH, with average discrepancies of about 15–20% in the CPT region (pressures 60–120 hPa) and larger overestimations (often exceeding 50%) at lower altitudes (corresponding to H₂O mixing ratios ≥ 20 ppmv, see Figure 4c). The only significant difference between the OPERA and ERA5 data sets consists of a slight dry bias of ERA5 compared to OPERA between 60 and 80 hPa in DK17, leading ERA5 to be in better agreement with CFH in the region of the H₂O maximum. In contrast to OPERA and ERA5, ERAI shows a large underestimation of UTLS H₂O relative to CFH for the interval 60–140 hPa, with discrepancies up to a factor of 2 or more at pressures 100–120 hPa, especially in DK17 (Figures 4b and 4c). At $p < 60$ hPa, all three ECMWF data sets reach good agreement with CFH, as the measured and modeled H₂O mixing ratios approach the background stratospheric value of 4–5 ppmv.

Interestingly, the nonmonotonic vertical distribution of H₂O in DK17 is well represented by OPERA and ERA5, though the H₂O minimum at the CPT is less pronounced, and the lower stratospheric maximum is

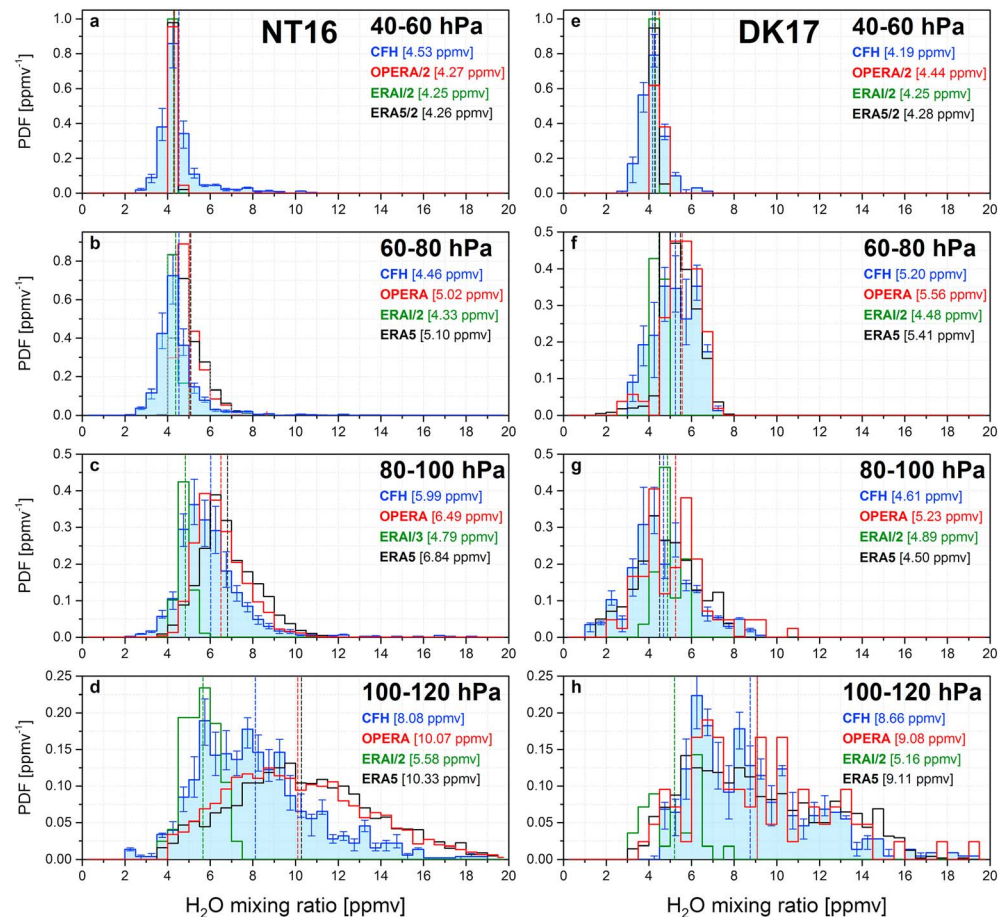


Figure 5. Probability density functions (PDFs) of H_2O mixing ratio from CFH (blue, with error bars calculated as described in section 4), OPERA (red), ERAI (green), and ERA5 (black) for pressure intervals 40–60 hPa (a, e), 60–80 hPa (b, f), 80–100 hPa (c, g), and 100–120 hPa (d, h), for the NT16 (a–d) and DK17 campaigns (e–h). (colored inserts) Mean values of the PDFs. Note that scaling by factors 2 or 3 are applied to the PDFs of OPERA, ERAI, and ERA5 in selected panels (noted in top right corner).

slightly shifted to higher altitudes (Figure 4b). This remarkably good agreement suggests that cycles 41R1 (used by ERA5) and 43R3 (OPERA) of the IFS model are able to capture the main dynamical and microphysical processes of the measurement period which determine the vertical distribution of UTLS H_2O , namely (most likely), overshooting convection hydrating the lower stratosphere (Brunamonti et al., 2018). Enhanced H_2O between approximately 70 and 100 hPa, attributed to the horizontal confinement effect of the ASM anticyclone (Brunamonti et al., 2018), is also well represented in OPERA and ERA5, despite the overestimation of CPT height. In contrast, the observed vertical distribution of UTLS H_2O in DK17 is not captured by ERAI, in which the minimum at the CPT and the maximum in the lower stratosphere are both absent. The fact that ERAI has two model levels at the altitudes of the H_2O minimum (approximately 88 hPa) and maximum (73 hPa), yet the observed H_2O structure is missing, suggests that this is not just due to lack of vertical resolution but is more likely related to less sophisticated cloud microphysics in IFS cycle 31R2 compared to 41R1 and 43R3 or to the lower horizontal resolution of ERAI. We also note that ERAI also misses the H_2O enhancement in the confined lower stratosphere in NT16, captured by all other data sets (80–90 hPa in Figure 4a), which may be related to the lower CPT altitude in ERAI.

4.2.2. PDFs

Figure 5 shows probability density functions (PDFs) of H_2O mixing ratio from CFH, OPERA, ERAI, and ERA5 for the NT16 (Figures 5a–5d) and DK17 (Figures 5e–5h) campaign periods, in four atmospheric pressure slabs of 20 hPa each between 40 and 120 hPa. The PDFs (in units of ppmv^{-1}) are calculated in 40 bins of

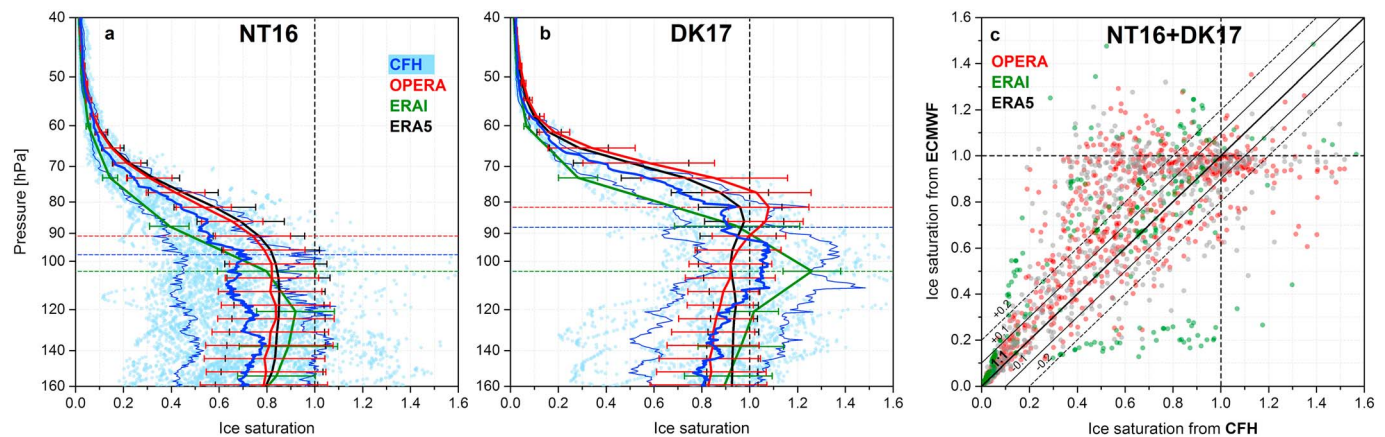


Figure 6. Ice saturation (S_{ice}) comparison of CFH measurements versus ECMWF data for the NT16 and DK17 campaigns. (a, b) All S_{ice} data points of CFH (dots), mean profile (thick blue solid line) and standard deviation of natural variability (thin blue lines), and mean profile and standard deviation bars of OPERA (red), ERAI (green), and ERA5 (black) as a function of pressure. Horizontal dashed lines show the pressure level of the average cold-point tropopause in the different data sets. (c) Scatter plot of S_{ice} from CFH versus OPERA (red dots), CFH versus ERAI (green), and CFH versus ERA5 (gray) for the NT16 and DK17 campaign periods. Horizontal black lines show the 1:1 correspondence line (thick solid) and S_{ice} discrepancies by ± 0.1 (thin solid) and ± 0.2 (thin dashed) between the model data and the measurements. Black dashed lines also mark the $S_{ice} = 1$ level in all panels.

width 0.5 ppmv between 0 and 20 ppmv, using model data from the entire campaign periods (i.e., same as in Figures 3a and 3b). For CFH measurements, we also show instrumental uncertainty bars along with the PDFs, which are based on the 10% uncertainty in H_2O mixing ratio determined by Vömel et al. (2007). The uncertainty bars are calculated by subdividing each bin of the PDFs into 10 subbins (of size 0.05 ppmv) and then adding the PDF values in the lowermost and uppermost subbin to the previous and following bin as upper limit of the uncertainty and subtracted from the PDF of the original bin as lower limit of the uncertainty.

The width of the PDFs calculated from OPERA and ERA5 data agrees generally well with those from CFH measurements, despite the slight wet bias discussed above, causing a shift toward high H_2O mixing ratios of the entire PDFs. This shows that both OPERA and ERA5 are able to correctly reproduce the natural variability of UTLS H_2O during the measurement periods. Conversely, the PDFs of ERAI are much too narrow and underestimate the frequency of occurrence of high H_2O mixing ratios compared to CFH. On average, for both campaign periods, OPERA and ERA5 overestimate H_2O mixing ratios measured by CFH by around 0.5–2.2 ppmv (decreasing with altitude) between 60 and 120 hPa, while ERAI exhibits underestimations as large as 3.5 ppmv. At lower pressures (40–60 hPa), all the three ECMWF data sets agree well with the measured H_2O mixing ratios, showing discrepancies smaller than 0.3 ppmv compared to CFH. However, the PDFs in all model data sets are narrower than those derived from CFH measurements (Figures 5a and 5e), suggesting that the natural variability of lower stratospheric H_2O is too weak in the ECMWF model. The mean values of each PDF shown in Figure 5 (noted in the colored insets of each panel) are also summarized in Table S1.

4.3. Ice Saturation (CFH vs. ECMWF)

Figures 6a and 6b shows all ice saturation (S_{ice}) measurements from CFH as a function of pressure (40–160 hPa), in comparison with mean profiles of ice saturation and its standard deviation ranges calculated from the OPERA, ERAI, and ERA5 data sets. The corresponding scatter plot of S_{ice} from CFH versus OPERA, ERAI, and ERA5 is shown in Figure 6c.

The interannual variability of UTLS S_{ice} between the years 2016 and 2017 is well captured by all three ECMWF products, showing lower ice saturations in NT16 and higher values in DK17 throughout the entire UTLS (Figures 6a and 6b). Such variability is mainly an effect of the different temperatures observed during the two campaign periods (Figure 3). In both cases, OPERA and ERA5 show a tendency to overestimate S_{ice} compared to the observations (see Figure 6c: the majority of red and black dots lies in the top-left quadrant of the scatter plot), which is expected in light of their moist bias showed in Figures 4 and 5 and their cold bias in

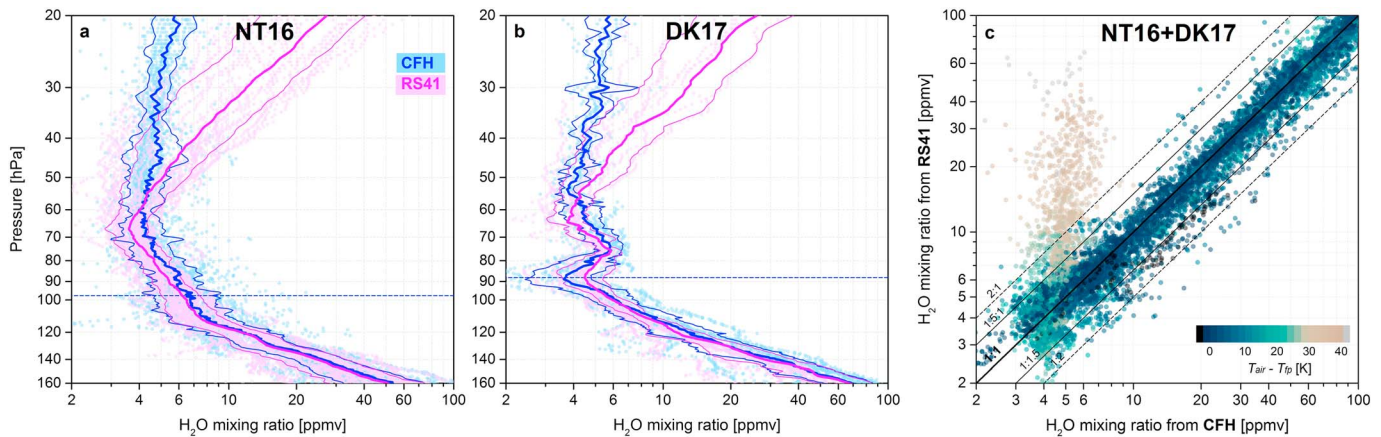


Figure 7. H₂O mixing ratio comparison of CFH versus RS41 measurements for the NT16 and DK17 campaigns. (a, b) All data points of H₂O mixing ratio (dots) and mean profiles (thick solid lines) and standard deviations of natural variability (thin solid lines) of CFH (blue) and RS41 (magenta) as a function of pressure. Blue dashed lines show the pressure level of the average cold-point tropopause in RS41 measurements. (c) Scatter plot of H₂O mixing ratio from CFH versus RS41, color-coded with the difference between air temperature (T_{air} , from RS41) and frostpoint temperature (T_{fp} , from CFH). Black lines show the 1:1 correspondence line (thick solid) and discrepancies by $\pm 50\%$ (i.e., 1:1.5 and 1:1.5, thin solid) and $\pm 100\%$ (i.e., 1:2 and 2:1, thin dashed) between the CFH and the RS41 measurements.

the lower stratosphere discussed in section 4.1. This applies to all altitudes except for 90–120 hPa in DK17, where S_{ice} from OPERA and ERA5 is smaller than for CFH, due to a slight warm bias of both data sets at these pressure levels (see Figure 3b). ERAI displays a systematic S_{ice} overestimation for $p < 100$ hPa and underestimation for $p > 100$ hPa, which reflects its cold/warm temperature biases discussed in section 4.1. The wide scatter of the ERAI versus CFH correlation (Figure 6c) suggests that the day-by-day variability of S_{ice} in the UTLS is not well captured by this data set.

In DK17, a local maximum with average $S_{\text{ice}} \approx 1$ is produced by all ECMWF products, although either too pronounced (as in ERAI) or shifted to lower pressure (OPERA and ERA5) compared to CFH. The upper tropospheric S_{ice} maximum at 100–120 hPa is higher in ERAI than in CFH measurements, which is consistent with the cold bias of ERAI at these pressure levels (Figure 3), and is likely the reason for its negative bias in H₂O mixing ratios discussed in section 4.2 (i.e., too strong dehydration occurring in this data set). The low bias of OPERA and ERA5 between 90 and 120 hPa is related to a slight warm bias of these data sets in this altitude range and campaign period, while better agreement between CFH and ERA5 compared to OPERA for $p < 90$ hPa in DK17 is due to the slight warm bias of ERA5 compared to OPERA in this region (see Figure 3b).

5. Instrumental Comparison

In this section we compare the water vapor measurements by CFH and RS41, first in terms of H₂O mixing ratio (section 5.1) and then in terms of ice saturation (section 5.2).

5.1. H₂O Mixing Ratio (CFH vs. RS41)

Similarly to the CFH/model comparison in Figure 4, Figure 7 shows all data points, mean profiles, and standard deviation ranges of H₂O mixing ratio from CFH and RS41 measurements for pressures 20–160 hPa (Figures 6a and 6b) and the corresponding scatter plots of H₂O mixing ratio from CFH versus RS41 (Figure 6c). Additionally, in Figure 7c, the data points are color-coded with the difference between air and frostpoint temperature, $T_{\text{air}} - T_{\text{fp}}$ (where T_{air} is derived from RS41 and T_{fp} from CFH measurements). PDFs of H₂O mixing ratio from CFH and RS41 measurements in four pressure intervals between 40 and 120 hPa (analogous to Figure 5 for the model comparison) are shown in Figure S3.

During both campaign periods, RS41 measurements show a very good agreement with CFH in the upper troposphere ($p > 100$ hPa), despite a slight dry bias of around 5% in average H₂O mixing ratio (Figures 7a and 7b). Around the CPT level (60–100 hPa), the dry bias of RS41 increases, reaching underestimations of $\approx 10\%$ (0.5 ppmv) in average H₂O mixing ratio and sometimes exceeding $\pm 50\%$ in individual flights (Figure 7c).

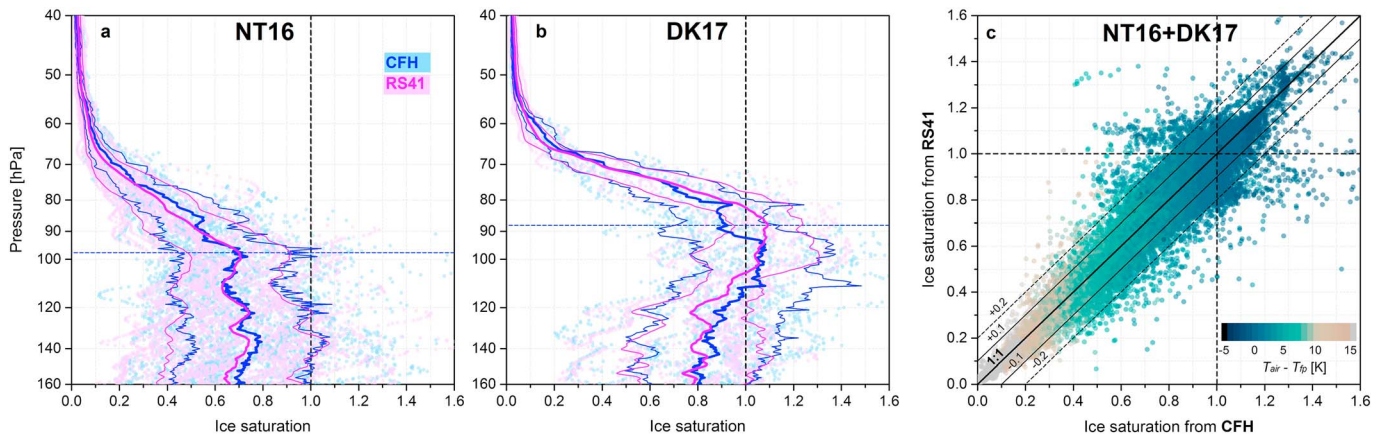


Figure 8. Ice saturation (S_{ice}) comparison of CFH versus RS41 measurements for the NT16 and DK17 campaigns. (a, b) All S_{ice} data points (dots) and mean profiles (thick solid lines) and standard deviations of natural variability (thin solid lines) of CFH (blue) and RS41 (magenta) as a function of pressure. Blue dashed lines show the pressure level of the average cold-point tropopause in RS41 measurements. (c) Scatter plot of S_{ice} from CFH versus RS41, color-coded with the difference between air temperature (T_{air} , from RS41) and frostpoint temperature (T_{fp} , from CFH). Horizontal black lines show the 1:1 correspondence line (thick solid) and S_{ice} discrepancies by ± 0.1 (thin solid) and ± 0.2 (thin dashed) between the CFH and the RS41 measurements. Black dashed lines also mark the $S_{ice} = 1$ level in all panels.

Such underestimation appears to be systematic (especially in NT16), suggesting that this must be due to a measurement or a calibration artifact, rather than just instrumental noise. In DK17, RS41 deviates from the dry bias in the region of the H_2O minimum at the CPT ($p \approx 90$ hPa), where higher H_2O mixing ratios by almost 1 ppmv are measured by RS41 than CFH. Conversely, in the region of the H_2O maximum ($p \approx 60$ – 80 hPa), RS41 shows a dry bias similar to that observed in NT16 at the same pressure level (Figure 7b). Overall, RS41 manages to capture the main features of the H_2O vertical distribution in both data sets, including the nonmonotonic mean profile of DK17.

At lower pressures (20–60 hPa), all RS41 measurements show an unrealistic increase with altitude of H_2O mixing ratios up to several tens of ppmv, hence strongly deviate from the ≈ 4 – 6 ppmv expected stratospheric background measured by CFH (Figures 7a and 7b). This artifact is expected for thin-film capacitive sensors, which cannot provide reliable measurements under such dry stratospheric conditions (see section 2). Rather, it is remarkable that the RS41 humidity measure stays on average within the $\approx 10\%$ error range up to about 2 km above the CPT. The pressure (altitude) where the RS41 mean profiles start drifting (i.e., showing a significantly different slope) from the mean profiles measured by CFH is around 65 hPa (≈ 19.5 km) in both campaign periods, while above 50 hPa (≈ 21 km), the two mean profiles start differing by more than one standard deviation of CFH. The color coding in Figure 7c reveals that deviations larger than 50% from the expected behavior in the RS41 measurements have onset at about $T_{air} - T_{fp} \approx 25$ K, while for $T_{air} - T_{fp} \geq 30$ K (approximately $p \leq 35$ hPa, see Figure 2a), nearly all measurements show discrepancies larger than 100% compared to CFH, suggesting that this is the upper limit of the measuring capability of the RS41 humidity sensor in the stratosphere (however, note that frostpoint depressions even larger than 30 K can be detected by RS41 in the troposphere, where absolute humidity is orders of magnitude larger than 4–6 ppmv). We also note that for $T_{air} - T_{fp} < -2$ K, most RS41 measurements underestimate H_2O mixing ratios by a factor of 1.5–2 with respect to CFH (see black dots in Figure 7c), suggesting that the RS41 sensor may be subject to a stronger dry bias during highly supersaturated conditions.

Finally, it should be remarked that the results discussed here apply to the subtropical stratosphere, where T_{air} and $T_{air} - T_{fp}$ increase rapidly above the CPT (Figure 2a), whereas the performances of RS41 may differ in middle and high latitudes, where the temperature increase above the CPT is smoother and RH decreases at a lower rate with altitude (e.g., Survo et al., 2015).

5.2. Ice Saturation (CFH vs. RS41)

Figures 8a and 8b show all measurements, mean profiles, and standard deviation ranges of ice saturation from CFH and RS41 as a function of pressure (40–160 hPa), while Figure 8c exhibits the corresponding

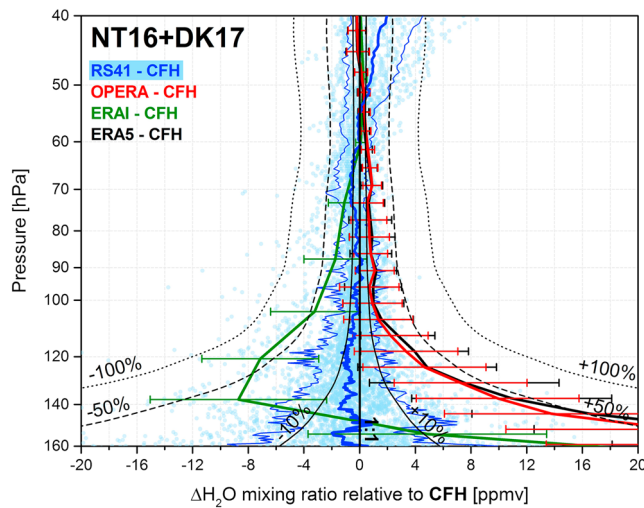


Figure 9. Mean profiles of H_2O mixing ratio difference ($\Delta\text{H}_2\text{O}$) relative to CFH calculated from a point-by-point comparison of the NT16 and DK17 campaigns combined, namely, RS41-CFH (light blue dots: all data, thick blue line: mean profile, thin blue solid lines: standard deviation), OPERA-CFH (red solid line: mean profile and standard deviation bars), ERAI-CFH (green solid line: mean profile and standard deviation bars), and ERA5-CFH (black solid line: mean profile and standard deviation bars). Black lines show the 1:1 correspondence level compared to CFH (i.e., perfect agreement: thick solid), 1:1.1 and 1.1:1 ratios (i.e., $\pm 10\%$ discrepancies, coinciding with the instrumental uncertainty of CFH measurements as determined by Vömel et al., 2007: thin solid), 1.5:1 and 1:1.5 ratios (i.e., $\pm 50\%$ deviation: thin dashed), and 2:1 and 1:2 ratios (i.e., $\pm 100\%$ deviation: thin dotted), calculated according to the mean CFH profile for both campaign periods together, smoothed by a moving average of ± 5 hPa.

scatter plot of S_{ice} from CFH versus S_{ice} from RS41. Analogously to Figure 7c, the scatter plot in Figure 8c is color-coded with $T_{\text{air}} - T_{\text{fp}}$ (however, note the different lower and upper boundaries of the two color scales).

Figures 8a and 8b show that RS41 measurements achieve an excellent representation of ice saturation throughout the entire UTLS, both in terms of average profiles and the extents of natural variability. In NT16, RS41 average S_{ice} values lie within a narrow ± 0.05 discrepancy range with respect to CFH, while larger discrepancies (up to ± 0.15) are observed in DK17. This may result from the lower temperature and therefore higher frequency of occurrence of highly supersaturated (i.e., likely in-cloud) samples in DK17 compared NT16, as discussed in the previous section. In particular, higher S_{ice} measured by RS41 near 90 hPa in DK17 is clearly related to the moist bias of RS41 in the region of the H_2O minimum (see Figure 8b). Interestingly, the mean S_{ice} profile by RS41 is similar to those simulated by the ECMWF OPERA and ERA5 data sets (see Figure 6b) that also overestimate H_2O in this region. For $p < 60$ hPa, the apparent agreement between RS41 and CFH is due to the low values of ice saturation in the stratosphere, masking the strong moist bias of RS41 shown in Figure 7. The point-by-point comparison in Figure 8c shows that nearly all data points in subsaturated conditions lie within a $\Delta S_{\text{ice}} = \pm 0.2$ difference between RS41 and CFH, whereas the discrepancies increase in supersaturated conditions. Although the bias seems to increase toward both larger underestimations and overestimations for $S_{\text{ice}} > 1$, we note that the frequency of occurrence of negatively biased samples in RS41 is larger than that of positively biased ones, with respect to CFH (i.e., more outlying data points are found in the bottom-right quadrant of Figure 8c than in the top-left one). It is also worth noting that a significant fraction of supersaturated measurements show no or little bias ($\Delta S_{\text{ice}} < \pm 0.1$) between RS41 and CFH up to S_{ice} as large as ≈ 1.4 (Figure 8c).

6. Summary

We have analyzed 38 high-quality measurements of UTLS H_2O performed by CFH in the ASM anticyclone region during the years 2016–2017 and used them to assess the performance of meteorological radiosondes (Vaisala RS41) and the quality of modeled UTLS H_2O from ECMWF operational (analysis and forecast combined: OPERA), ERA-Interim reanalysis, and the newly released ERA5 reanalysis data sets. For a summary, we combine the NT16 and DK17 observational data sets and quantify the overall H_2O mixing ratio differences ($\Delta\text{H}_2\text{O}$) of the RS41, OPERA, ERAI, and ERA5 data sets with respect to CFH. Mean profiles and standard deviation ranges of $\Delta\text{H}_2\text{O}$ for RS41-CFH, OPERA-CFH, ERAI-CFH, and ERA5-CFH are shown in Figure 9, while the mean values of $\Delta\text{H}_2\text{O}$ in four selected pressure bins (expressed both as absolute values and percent units) are summarized in Table 2. Note that $\Delta\text{H}_2\text{O}$ is calculated only for model time steps coincident with CFH soundings and simultaneous CFH-RS41 measurements.

ECMWF operational and ERA5 data systematically overestimate H_2O mixing ratios compared to CFH over the entire UTLS (Figure 9). Considering the combined data set shown in Figure 9, the moist bias of OPERA and ERA5 is 23–27% (2–2.3 ppmv) in the upper troposphere (100–120 hPa) and 14–17% around the tropopause (0.7–0.9 ppmv for 60–100 hPa; see Table 2). In the lower stratosphere (40–60 hPa), H_2O mixing ratios from OPERA and ERA5 fall within a $\pm 4\%$ (± 0.2 ppmv) discrepancy with respect to the CFH measurements, which is smaller than the CFH instrumental uncertainty, yet the natural variability of H_2O observed by CFH in this pressure range is significantly underestimated by the model (Figures 5a and 5b). In contrast to OPERA and ERA5, ERA-Interim data show a strong underestimation of H_2O in the upper troposphere, differing from CFH on average by 38% (3.2 ppmv) for pressures 100–120 hPa and more than 50% for $p > 120$ hPa. The underestimation decreases with altitude to 14–30% (0.6–1.7 ppmv) for pressures 60–100 hPa, and

Table 2
Summary of H₂O Mixing Ratio Comparison

Pressure bin (hPa)	OPERA-CFH	ERA5-CFH	ERA-Interim-CFH	RS41-CFH
40–60	+0.20 ppmv (+4%)	+0.13 ppmv (+3%)	+0.46 ppmv (+10%)	+0.63 ppmv (+14%)
60–80	+0.67 ppmv (+14%)	+0.72 ppmv (+15%)	−0.64 ppmv (−14%)	−0.41 ppmv (−9%)
80–100	+0.83 ppmv (+15%)	+0.94 ppmv (+17%)	−1.68 ppmv (−30%)	−0.16 ppmv (−3%) ^a
100–120	+1.97 ppmv (+23%)	+2.32 ppmv (+27%)	−3.23 ppmv (−38%)	−0.51 ppmv (−6%)

Note. Average H₂O mixing ratio difference (in ppmv) and relative difference (percentage, in brackets) for each dataset (CFH, OPERA, ERAI, and RS41) relative to CFH for the combined NT16 + DK17 data set (as shown in Figure 8), in four selected pressure bins.

^aThe 3% net dry bias of RS41 at 80–100 hPa results from the combination of a larger dry bias in NT16 and a moist bias in DK17 (see Figure 6).

as for OPERA and ERA5, the agreement with CFH falls within a discrepancy equal or smaller than the instrumental uncertainty ($\pm 10\%$) at higher altitudes in the stratosphere (40–60 hPa).

The moist bias of the ECMWF operational data in the UTLS is consistent with the findings of Dyroff et al. (2015; using IFS model cycles from 29R1 to 38R1), although their comparison was limited to altitudes between 9 and 12 km and in contrast to those of Kunz et al. (2014) (using IFS model cycles from 23R4 to 37R3), who reported a dry bias of ECMWF operational data in the tropical and extratropical UTLS (however, no measurements from the ASM anticyclone region were contained in their analysis). Our early evaluation of the newly released ERA5 reanalysis shows that this data set provides an overall more accurate representation of UTLS H₂O compared to ERA-Interim, in terms of water vapor concentration as well as its vertical distribution and short-term natural variability. Based on this result, we recommend modeling studies using ECMWF reanalysis data to investigate water vapor in the ASM anticyclone to dismiss the use of ERA-Interim in favor of the newer ERA5 reanalysis data set. Furthermore, these studies should account for the fact that a moist bias in UTLS H₂O is to be expected in ECMWF products based on IFS model cycles 41R1–43R3 (including ERA5), whereas a dry bias is to be expected in ERA-Interim (IFS cycle 31R2) humidity data.

RS41 humidity measurements show an average slight underestimation of H₂O mixing ratios for all pressures $p > 60$ hPa (Figure 9), namely, of 3–6% (0.1–0.5 ppmv) for 80–120 hPa and 9% (0.4 ppmv) for 60–80 hPa (see Table 2) compared to CFH. Although deviations as large as $\pm 50\%$ may occur in single measurements (Figure 8), the RS41 data manage to capture the main features of the vertical distributions of UTLS H₂O observed by CFH up to approximately $p \approx 65$ hPa (see Figure 7). Above this level (altitude ≈ 19.5 km, roughly corresponding to 2 km above the CPT), RS41 strongly overestimates H₂O mixing ratios compared to CFH (+14% on average at 40–60 hPa and more than a factor of 2 for $p < 40$ hPa) due to the known measurement artifacts of the thin-film capacitive sensors discussed in section 2. Despite this is a more promising result than the Arctic comparison by Survo et al. (2015), it shows that thin-film capacitive detectors remain unsuitable for stratospheric water vapor measurements, which require more sophisticated instruments such as frostpoint hygrometers.

Acknowledgments

The research leading to these results has received funding from the European Community's Seventh Framework Programme (FP7/2007–2013) under grant agreement 603557 and the Swiss National Science Foundation in project 200021-147127. The use of ECMWF data is gratefully acknowledged. The authors thank Hannu Jauhiainen from Vaisala Oyj (Finland) for technical support and Michael Sprenger for valuable discussion. Support from the HiCCDRC group of Rijan Kayastha at Kathmandu University is highly acknowledged for the observations at Dhulikhel.

Data Availability

The observational data underlying this research can be found in the paper's supporting information. The ECMWF data can be accessed online (<https://apps.ecmwf.int/datasets/>).

References

- Bergman, J. W., Fierli, F., Jensen, E. J., Honomichl, S., & Pan, L. L. (2013). Boundary layer sources for the Asian anticyclone: Regional contributions to a vertical conduit. *Journal of Geophysical Research: Atmospheres*, 118, 2560–2575. <https://doi.org/10.1002/jgrd.50142>
- Brewer, A. W. (1949). Evidence for a world circulation provided by the measurements of helium and water vapour distribution in the stratosphere. *Quarterly Journal of the Royal Meteorological Society*, 75(326), 351–363. <https://doi.org/10.1002/qj.49707532603>
- Brewer, A. W., & Dobson, R. H. (1951). An automatic frost-point hygrometer for measurements in the upper air. *Proceedings of the Institute of Electrical and Electronics Engineers*, 98(64), 470–473.
- Brunamonti, S., Jorge, T., Oelsner, P., Hanumanthu, S., Singh, B. B., Kumar, K. R., et al. (2018). Balloon-borne measurements of temperature, water vapor, ozone and aerosol backscatter at the southern slopes of the Himalayas during StratoClim 2016–2017. *Atmospheric Chemistry and Physics*, 18(21), 15,937–15,957. <https://doi.org/10.5194/acp-18-15937-2018>

- Dee, D. P., Uppala, S. M., Simmons, A. J., Berrisford, P., Poli, P., Kobayashi, S., et al. (2011). The ERA-Interim reanalysis: Configuration and performance of the data assimilation system. *Quarterly Journal of the Royal Meteorological Society*, 137(656), 553–597. <https://doi.org/10.1002/qj.828>
- Dirksen, R. J., Sommer, M., Immler, F. J., Hurst, D. F., Kivi, R., & Vömel, H. (2014). Reference quality upper-air measurements: GRUAN data processing for the Vaisala RS92 radiosonde. *Atmospheric Measurement Techniques*, 7(12), 4463–4490. <https://doi.org/10.5194/amt-7-4463-2014>
- Dyroff, C., Zahn, A., Christner, E., Forbes, R. M., Tompkins, A. M., & van Velthoven, P. F. J. (2015). Comparison of ECMWF analysis and forecast humidity data to CARIBIC upper troposphere and lower stratosphere observations. *Quarterly Journal of the Royal Meteorological Society*, 141(688), 833–844. <https://doi.org/10.1002/qj.2400>
- ECMWF (2018). What are the differences changes from ERA-Interim to ERA5? <https://confluence.ecmwf.int/pages/viewpage.action?pageId=74764925> (accessed 18 February 2019)
- Fadnavis, S., Semeniuk, K., Pozzoli, L., Schultz, M. G., Ghude, S. D., Das, S., & Kakaktar, R. (2013). Transport of aerosols into the UTLS and their impact on the Asian monsoon region as seen in a global model simulation. *Atmospheric Chemistry and Physics*, 13(17), 8771–8786. <https://doi.org/10.5194/acp-13-8771-2013>
- Fahey, D. W., Gao, R.-S., Möhler, O., Saathoff, H., Schiller, C., Ebert, V., et al. (2014). The AquaVIT-1 intercomparison of atmospheric water vapor measurement techniques. *Atmospheric Measurement Techniques*, 7(9), 3177–3213. <https://doi.org/10.5194/amt-7-3177-2014>
- Fu, R., Hu, Y., Wright, J. S., Jiang, J. E., Dickinson, R. E., Chen, M., et al. (2006). Short circuit of water vapor and polluted air to the global stratosphere by convective transport over the Tibetan plateau. *Proceedings of the National Academy of Sciences of the United States of America*, 103(15), 5664–5669. <https://doi.org/10.1073/pnas.0601584103>
- Fueglistaler, S., Bonazzola, M., Haynes, P. H., & Peter, T. (2005). Stratospheric water vapor predicted by the Lagrangian temperature history of air entering the stratosphere in the tropics. *Journal of Geophysical Research*, 110, D08107. <https://doi.org/10.1029/2004JD005516>
- Garny, H., & Randel, W. (2016). Transport pathways from the Asian monsoon anticyclone to the stratosphere. *Atmospheric Chemistry and Physics*, 16(4), 2703–2718. <https://doi.org/10.5194/acp-16-2703-2016>
- Hall, E. G., Jordan, A. F., Hurst, D. F., Oltmans, S. J., Vömel, H., Kühnreich, B., & Ebert, V. (2016). Advancements, measurement uncertainties, and recent comparisons of the NOAA frost point hygrometer. *Atmospheric Measurement Techniques*, 9(9), 4295–4310. <https://doi.org/10.5194/amt-9-4295-2016>
- Hardy, B. (1998). ITS-90 Formulations for vapor pressure, frostpoint temperature, dewpoint temperature, and enhancement factors in the range –100 to +100 °C. The Proceedings of the Third International Symposium on Humidity & Moisture, London, England.
- Heath, N. K., & Fuelberg, H. E. (2014). Using a WRF simulation to examine regions where convection impacts the Asian monsoon anticyclone. *Atmospheric Chemistry and Physics*, 14(4), 2055–2070. <https://doi.org/10.5194/acp-14-2055-2014>
- Hegglin, M. I., Tegtmeier, S., Anderson, J., Froidevaux, L., Fuller, R., Funke, B., et al. (2013). SPARC Data Initiative: Comparison of water vapor climatologies from international satellite limb sounders. *Journal of Geophysical Research: Atmospheres*, 118, 11,824–11,846. <https://doi.org/10.1002/jgrd.50752>
- Holton, J. R., Haynes, P. H., McIntyre, M. E., Douglass, A. R., Rood, R. B., & Pfister, L. (1995). Stratosphere-troposphere exchange. *Reviews of Geophysics*, 33(4), 403–439. <https://doi.org/10.1029/95RG02097>
- Hurst, D. F., Oltmans, S. J., Vömel, H., Rosenlof, K. H., Davis, S. M., Ray, E. A., et al. (2011). Stratospheric water vapor trends over Boulder, Colorado: Analysis of the 30 year Boulder record. *Journal of Geophysical Research*, 116, D02306. <https://doi.org/10.1029/2010JD015065>
- Jachowicz, R. S., & Senturia, S. D. (1981). A thin-film capacitance humidity sensor. *Sensors and Actuators*, 2, 171–186. [https://doi.org/10.1016/0250-6874\(81\)80036-4](https://doi.org/10.1016/0250-6874(81)80036-4)
- Jensen, E. J., Kärcher, B., Ueyama, R., Pfister, L., Bui, T. V., Diskin, G. S., et al. (2018). Heterogeneous ice nucleation in the tropical tropopause layer. *Journal of Geophysical Research: Atmospheres*, 123, 12,210–12,227. <https://doi.org/10.1029/2018JD028949>
- Krämer, M., Schiller, C., Afchine, A., Bauer, R., Gensch, L., Mangold, A., et al. (2009). Ice supersaturations and cirrus cloud crystal numbers. *Atmospheric Chemistry and Physics*, 9(11), 3505–3522. <https://doi.org/10.5194/acp-9-3505-2009>
- Krishnamurti, T. N., & Bhalme, H. N. (1976). Oscillations of a monsoon system. Part I. Observational aspects. *Journal of the Atmospheric Sciences*, 33(10), 1937–1954. [https://doi.org/10.1175/1520-0469\(1976\)033<1937:OAMSP>2.0.CO;2](https://doi.org/10.1175/1520-0469(1976)033<1937:OAMSP>2.0.CO;2)
- Kunz, A., Spelten, N., Konopka, P., Müller, R., Forbes, R. M., & Wernli, H. (2014). Comparison of Fast In situ Stratospheric Hygrometer (FISH) measurements of water vapor in the upper troposphere and lower stratosphere (UTLS) with ECMWF (re)analysis data. *Atmospheric Chemistry and Physics*, 14(19), 10803–10822. <https://doi.org/10.5194/acp-14-10803-2014>
- Mastenbrook, H. J., & Dinger, J. E. (1961). Distribution of water vapor in the stratosphere. *Journal of Geophysical Research*, 66(5), 1437–1444. <https://doi.org/10.1029/JZ066i005p01437>
- Miloshevich, L. M., Vömel, H., Whitemann, D. N., & Leblanc, T. (2009). Accuracy assessment and correction of Vaisala RS92 radiosonde water vapor measurements. *Journal of Geophysical Research*, 114, D11305. <https://doi.org/10.1029/2008JD011565>
- Mote, P. W., Rosenlof, K. H., McIntyre, M. E., Carr, E. S., Gille, J. C., Holton, J. R., et al. (1996). An atmospheric tape recorder: The imprint of tropical tropopause temperatures on stratospheric water vapor. *Journal of Geophysical Research*, 101(D2), 3989–4006. <https://doi.org/10.1029/95JD03422>
- Murphy, D. M., & Koop, T. (2005). Review of the vapour pressures of ice and supercooled water for atmospheric applications. *Quarterly Journal of the Royal Meteorological Society*, 131(608), 1539–1565. <https://doi.org/10.1256/qj.04.94>
- Newell, R. E., & Gould-Stewart, S. (1981). A stratospheric fountain? *Journal of the Atmospheric Sciences*, 38(12), 2789–2796. [https://doi.org/10.1175/1520-0469\(1981\)038<2789:ASF>2.0.CO;2](https://doi.org/10.1175/1520-0469(1981)038<2789:ASF>2.0.CO;2)
- Pan, L. L., Honomichl, S. B., Kinnison, D. E., Abalos, M., Randel, W. J., Bergman, J. W., & Bian, J. (2016). Transport of chemical tracers from the boundary layer to stratosphere associated with the dynamics of the Asian summer monsoon. *Journal of Geophysical Research: Atmospheres*, 121, 14,159–14,174. <https://doi.org/10.1002/2016JD025616>
- Pan, L. L., Paulik, L. C., Honomichl, S. B., Munchak, L. A., Bian, J., Selkirk, H. B., & Vömel, H. (2014). Identification of the tropical tropopause transition layer using the ozone-water vapor relationship. *Journal of Geophysical Research: Atmospheres*, 119, 3586–3599. <https://doi.org/10.1002/2013JD020558>
- Park, M., Randel, W. J., Gettelman, A., Massie, S. T., & Jiang, J. H. (2007). Transport above the Asian summer monsoon anticyclone inferred from Aura Microwave Limb Sounder tracers. *Journal of Geophysical Research*, 112, D16309. <https://doi.org/10.1029/2006JD008294>
- Petzold, A., Krämer, M., Neis, P., Rolf, C., Rohs, S., Berkes, F., et al. (2017). Upper tropospheric water vapour and its interaction with cirrus clouds as seen from IAGOS long-term routine in situ observations. *Faraday Discussions*, 200, 229–249. <https://doi.org/10.1039/c7fd00006e>

- Randel, W. J., & Park, M. (2006). Deep convective influence on the Asian summer monsoon anticyclone and associated tracer variability observed with Atmospheric Infrared Sounder (AIRS). *Journal of Geophysical Research*, 111, D12314. <https://doi.org/10.1029/2005JD006490>
- Randel, W. J., Park, M., Emmons, L., Kinnison, D., Bernath, P., Walker, K. A., et al. (2010). Asian monsoon transport of pollution to the stratosphere. *Science*, 328(5978), 611–613. <https://doi.org/10.1126/science.1182274>
- Randel, W. J., Wu, F., Gettelman, A., Russel, J. M. III, Zawodny, J. M., & Oltmans, S. J. (2001). Seasonal variation of water vapor in the lower stratosphere observed in Halogen Occultation Experiment data. *Journal of Geophysical Research*, 106, 14,313–14,325. <https://doi.org/10.1029/2001JD900048>
- Riese, M., Ploeger, F., Rap, A., Vogel, B., Konopka, P., Dameris, M., & Forster, P. (2012). Impacts of uncertainties in atmospheric mixing on simulated UTLS composition and related radiative effects. *Journal of Geophysical Research*, 117, D16305. <https://doi.org/10.1029/2012JD017751>
- Rosenlof, K. H., Oltmans, S. J., Kley, D., Russell, J. M. III, Chiou, E.-W., Chu, W. P., et al. (2001). Stratospheric water vapor increases over the past half-century. *Geophysical Research Letters*, 28(7), 1195–1198. <https://doi.org/10.1029/2000GL012502>
- Solomon, S., Rosenlof, K. H., Portman, R. W., Daniel, J. S., Davis, S. M., Sanford, F. J., & Plattner, G.-K. (2010). Contributions of stratospheric water vapor to decadal changes in the rate of global warming. *Science*, 327(5970), 1219–1223. <https://doi.org/10.1126/science.1182488>
- Suomi, V. E., & Barret, E. W. (1952). An experimental radiosonde for the investigation of the distribution of water vapor in the stratosphere. *Review of Scientific Instruments*, 23(6), 272–292. <https://doi.org/10.1063/1.1746250>
- Survo, P., Leblanc, T., Kivi, R., Jauhainen, H., & Lehtinen, R. (2015). Comparison of selected in-situ and remote sensing technologies for atmospheric humidity measurements. Manuscript 13B.2 presented at the 95th American Meteorological Society (AMS) Annual Meeting, <https://ams.confex.com/ams/95Annual/webprogram/Paper255790.html> (accessed 12 November 2018)
- Thölix, L., Backman, L., Kivi, R., & Karpechko, A. Y. (2016). Variability of water vapour in the Arctic stratosphere. *Atmospheric Chemistry and Physics*, 16(7), 4307–4321. <https://doi.org/10.5194/acp-16-4307-2016>
- Tompkins, A. M., Gierens, K., & Radel, G. (2007). Ice supersaturation in the ECMWF integrated forecast system. *Quarterly Journal of the Royal Meteorological Society*, 133(622), 53–63. <https://doi.org/10.1002/qj.14>
- Vaisala (2014). VaisalaDigiCORA Sounding System MW41, Technical Reference, Vaisala Oyi, P.O. Box 26, FI 00421, Helsinki, Finland. <http://meteorology.lyndonstate.edu/-/ATM/wp-content/uploads/2015/05/M211415EN-F.pdf> (accessed 4 January 2018)
- Vaisala (2017). Vaisala Radiosonde RS41 Measurement Performance, White Paper, Vaisala, P.O. Box 26, FI 00421, Helsinki, Finland. <https://www.vaisala.com/sites/default/files/documents/WEA-MET-RS41-Performance-White-paper-B211356EN-B-LOW-v3.pdf> (accessed 4 January 2018)
- Vaughan, G., Schiller, C., MacKenzie, A. R., Bower, K., Peter, T., Schlager, H., et al. (2008). SCOUTO3/ACTIVE High-altitude aircraft measurements around deep tropical convection. *Bulletin of the American Meteorological Society*, 89(5), 647–662. <https://doi.org/10.1175/BAMS-89-5-647>
- Vellere, R. K., Kaplan, M. L., Krishnan, R., Lewis, J. M., Sabade, S., Deshpande, N., et al. (2016). Monsoon-extratropical circulation interactions in Himalayan extreme rainfall. *Climate Dynamics*, 46(11–12), 3517–3546. <https://doi.org/10.1007/s00382-015-2784-x>
- Vérèmes, H., Keckhut, P., Baray, J.-L., Cammas, J.-P., Dionisi, D., Payen, G., et al. (2016). Water vapor profiles up to the UT/LS from Raman lidar at Reunion Island (21°S, 55°E): technical description, data processing and comparison with sondes. *European Physical Journal*, 119, 05004. <https://doi.org/10.1051/epjconf/201611905004>
- Vömel, H., David, D. E., & Smith, K. (2007). Accuracy of tropospheric and stratospheric water vapor measurements by the cryogenic frost point hygrometer: Instrumental details and observations. *Journal of Geophysical Research*, 112, D08305. <https://doi.org/10.1029/2006JD007224>
- Vömel, H., Naebert, T., Dirksen, R., & Sommer, M. (2016). An update on the uncertainties of water vapor measurements using Cryogenic Frostpoint Hygrometers. *Atmospheric Measurement Techniques*, 9(8), 3755–3768. <https://doi.org/10.5194/amt-9-3755-2016>
- Vömel, H., Oltmans, S. J., Hofmann, D. J., Deshler, T., & Rosen, J. M. (1995). The evolution of the dehydration in the Antarctic stratospheric vortex. *Journal of Geophysical Research*, 100(D7), 13,919–13,926. <https://doi.org/10.1029/95JD01000>
- Vömel, H., Oltmans, S. J., Johnson, B. J., Hasebe, F., Shiotani, M., Fujiwara, M., et al. (2002). Balloon-borne observations of water vapor and ozone in the tropical upper troposphere and lower stratosphere. *Journal of Geophysical Research*, 107(D14), 4210. <https://doi.org/10.1029/2001JD000707>
- von Hobe, M., Bekki, S., Borrmann, S., Cairo, F., D'Amato, F., di Donfrancesco, G., et al. (2013). Reconciliation of essential process parameters for an enhanced predictability of Arctic stratospheric ozone loss and its climate interactions (RECONCILE): Activities and results. *Atmospheric Chemistry and Physics*, 13(18), 9233–9268. <https://doi.org/10.5194/acp-13-9233-2013>
- Wexler, A. (1976). Vapor pressure formulation for water in range 0 to 100°C. A Revision. *Journal of Research of the National Bureau of Standards*, 80A(5–6), 775–785. <https://doi.org/10.6028/jres.080A.071>